EPJ Web of Conferences **79**, 01007 (2014)
DOI: 10.1051/epjconf/20147901007

Transport analysis of high radiation and high density plasmas in the ASDEX Upgrade tokamak

L. Casali, M. Bernert, R. Dux, R. Fischer, A. Kallenbach, B. Kurzan, P. Lang, A. Mlynek, R.M. McDermott, F. Ryter, M. Sertoli, G. Tardini, H. Zohm and the ASDEX Upgrade Team

Max-Planck-Institut für Plasmaphysik, Bolzmannstr. 2, 85748 Garching, Germany

Abstract. Future fusion reactors, foreseen in the "European road map" such as DEMO, will operate under more demanding conditions compared to present devices. They will require high divertor and core radiation by impurity seeding to reduce heat loads on divertor target plates. In addition, DEMO will have to work at high core densities to reach adequate fusion performance. The performance of fusion reactors depends on three essential parameters: temperature, density and energy confinement time. The latter characterizes the loss rate due to both radiation and transport processes. The DEMO foreseen scenarios described above were not investigated so far, but are now addressed at the ASDEX Upgrade tokamak. In this work we present the transport analysis of such scenarios. Plasma with high radiation by impurity seeding: transport analysis taking into account the radiation distribution shows no change in transport during impurity seeding. The observed confinement improvement is an effect of higher pedestal temperatures which extend to the core via stiffness. A non coronal radiation model was developed and compared to the bolometric measurements in order to provide a reliable radiation profile for transport calculations. High density plasmas with pellets: the analysis of kinetic profiles reveals a transient phase at the start of the pellet fuelling due to a slower density build up compared to the temperature decrease. The low particle diffusion can explain the confinement behaviour.

1. Introduction

The designs of future fusion reactors like ITER and DEMO are based on present tokamaks with a poloidal divertor. The control of particle and power exhaust is, to a large extent, concentrated in the divertor region. To limit the power load on the machine components to a tolerable level, a fraction of this power should be radiated in the divertor volume. This can be achieved by introducing a controlled small amount of appropriate impurities into the plasma. This technique is named impurities seeding and will be mandatory in future devices. It is sometimes already required in present machines and is extensively investigated in view of future reactors. Thereby nitrogen is an adequate impurity for edge and divertor radiation. The high confinement mode (H-mode) [1], which is the mostly used plasma regime in present divertor tokamaks, is also envisaged for future reactors. In H-mode, the formation of an edge transport barrier provides high temperatures and densities leading to the so-called pedestal, characterized by very steep edge pressure gradients. Under such conditions regular magneto-hydrodynamics instabilities, the

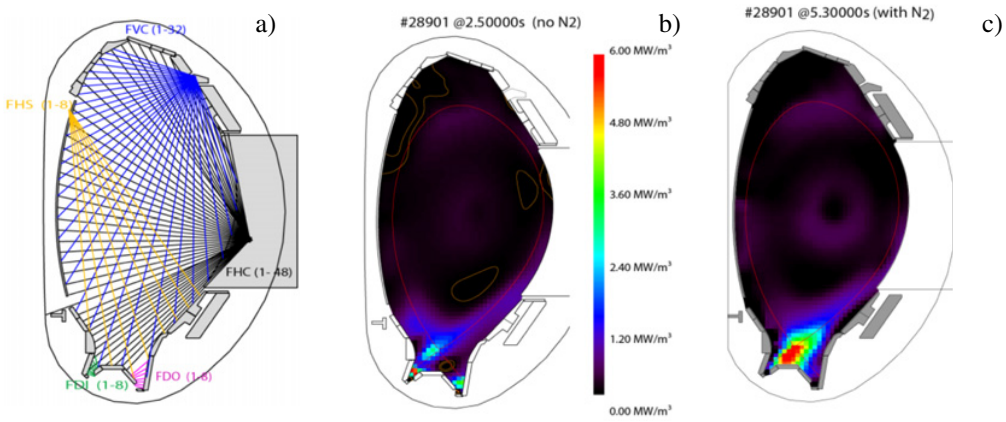

Figure 1. Cross section of ASDEX Upgrade. a) Lines of sight of the cameras used for the tomography reconstruction. b) 2D poloidal emissivity distribution without nitrogen seeding. c) 2D poloidal emissivity distribution with nitrogen seeding. Note the high radiation level in the divertor (red spot). The radiative ring in the centre is an artefact of the tomography reconstruction.

Edge Localized Modes (ELMs) occur [2]. Each ELM expels a significant amount of particles and energy from the pedestal during its short (≈1 ms) "crash". The pedestal is then re-established on a longer time scale. The work presented here has been carried out in ASDEX Upgrade (AUG), a medium size tokamak with full metallic wall. In fact since 2007 all plasma facing components are tungsten-coated [3]. Divertor cooling by nitrogen seeding has been extensively investigated, see e.g. [4]. Thereby a confinement increase due to the presence of nitrogen has been discovered [5, 6]. The analysis of the radiative power and the transport properties of H-modes under such conditions is presented in the next two sections. Future reactors will also operate at very high density to maximize the fusion power. Such scenarios have been investigated in AUG [7] and the transport results are discussed in Sect. 3.

2. Radiation in fusion plasmas

The radial radiation distribution of the electromagnetic radiated power is an essential component of the power balance in tokamaks. It will be even more important in fusion reactors where a non-negligible fraction of the energy will have to be dissipated through radiation. The main contributors to the plasma radiation due to the ions are bremsstrahlung, line and recombination radiation. The electron cyclotron emission can be neglected in the total power losses in present devices, but will contribute in reactors [8]. The presence of impurities in the plasma has a significant impact on fusion performance through dilution of the man ions and radiation losses. The sources of impurities in a tokamak are the plasma-wall interaction processes and the deliberate injection for diagnostic purpose or for radiative cooling. In this section we focus on radiation and discuss measurements and modelling.

2.1 Radiation measurements by bolometry

At ASDEX Upgrade the radiation is measured by several foil bolometer cameras mounted at different locations in the vessel as shown in Fig. 1a. The bolometers measure the radiative power emitted along 112 lines of sight. The line of sight grid enables to retrieve a 2D poloidal radiation distribution as shown in Figs. 1b and 1c.

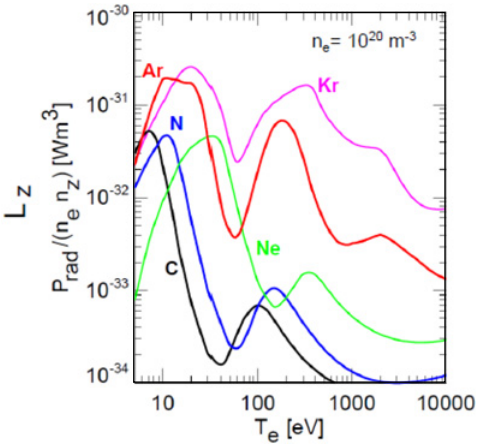

Figure 2. Cooling rate Lz as sum of bremmstrahlung, recombination and line radiation from ADAS for seed impurities close to coronal equilibrium.

Details on bolometric tomography are reported in reference [9]. Figure 1b shows the 2D radiation distribution before the nitrogen seeding. Here a rather weak radiation is detected in the divertor region and no strong radiation in the main plasma. Figure 1c shows the 2D radiation distribution of the same discharge during nitrogen seeding. Nitrogen is an efficient divertor and edge radiator (see Sect. 2.2), therefore an increased radiation in the scrape of layer and a very strong localised radiation in the divertor are found. The radiative ring visible in the core region is an artefact of the tomography which is attributed to the limited spatial resolution of the bolometry system and to the divertor radiation.

2.2 Theoretical background and modelling: Coronal and non-coronal equilibrium

The impurities enter the plasma as neutrals and are ionized depending on the plasma temperature. They penetrate up to the plasma center or leave the plasma depending on the transport properties. The main contribution to radiation comes from non-fully stripped ions during the ionization processes. For low Z impurities such as nitrogen or carbon, ionization takes place at the plasma edge, while for higher Z impurities, such as tungsten, it occurs over the whole cross-section. When the transport processes are slow enough, the ionisation stages of the impurities are in equilibrium corresponding to the plasma temperature. This situation is denoted coronal equilibrium and occurs in the plasma core. Corrections must be made if transport plays a role and this equilibrium is not reached as happens for instance in the plasma edge.

The radiative power for a given impurity is calculated using atomic data and a collisional radiative model. This model solves the time-dependent ionization equations as the sum of bremsstrahlung, line radiation, recombination and ionization contributions [10]. Hereby the so-called cooling factors $L_z(T_e)$ [11], yielded by the Atomic Data and Structure Analysis (ADAS) database [12] are used. As illustrated in Fig. 2, assuming coronal equilibrium, the low-Z impurities, such as N and C, radiate at low temperature and are therefore suitable elements for edge and divertor radiation. Impurities with higher Z number like Ar and Kr radiate significantly up to high temperatures and can therefore be used as main plasma radiators. Tungsten radiates strongly up to about 10 keV [13]. The local radiation power density is given by the product $L_z \cdot n_e^2 \cdot c_z$ where n_e is the electron density and c_z the impurity concentration.

At the plasma edge, in particular where ELMs regularly expel particles, transport effects play a key role and the coronal equilibrium assumption is not valid. The determination of the radiated power density must then take into account the impurity residence time, τ, as well as the time evolution of the

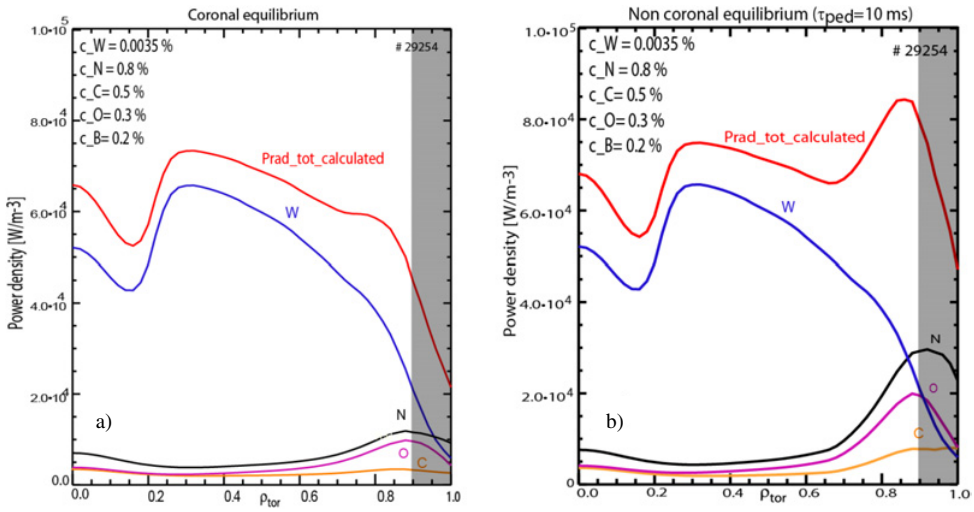

Figure 3. Prediction of the radiated power density: a) coronal conditions, b) non coronal conditions. Shown are the calculated radiated powers from carbon (orange), from oxygen (magenta), from nitrogen (black) and from tungsten (blue). The sum of the radiated powers, P_{rad_tot}, is shown in red. The comparison shows that if the non coronal effects are neglected, the radiated power at the edge is significantly underestimated.

plasma parameters and impurity influx. Non-coronal conditions mostly lead to an enhancement of the radiated power during the ionization to the equilibrium charge state. In this phase radiation increases for decreasing values of τ. The coronal equilibrium corresponds to large value of τ [14]. For the non-coronal radiation calculations one assumes that impurities enter in the plasma as neutrals [10] and emit line radiation during the early ionisation phase. The enhanced radiation due to the non-coronal effects is usually described using the parameter $n_e \cdot \tau$, such that L_z depends on both T_e and $n_e \cdot \tau$. Their values are provided by the ADAS database. In the calculation of the radial profiles of L_z for each impurity, T_e and n_e are taken from the experimental profiles whereas τ has to be determined as follows. In the pedestal the ELMs flush out impurities and cause a reorganization of the profiles at every crash. The residence time cannot exceed the inverse of the ELM frequency $1/f_{ELM}$. Furthermore, an appropriate function for τ must depend on the radius and satisfy two conditions: in the core τ must be long to reflect the coronal equilibrium ($n_e \cdot \tau = 10^{22}\,m^{-3}\,ms$) and then decrease to a small value, τ_{ped}, in the edge region. The hyperbolic tangent fulfils these constraints and a good agreement with the experimental radiative power is provided using the following formula:

$$\tau = 100 \cdot \left(- \tan h(k \cdot (\rho_{tor} - \rho_{crit}))) + \frac{1}{2} \right) + \tau_{ped}. \quad (1)$$

In the formula the factor 100 is required to reach coronal values in the core, k characterizes the slope of the tangent hyperbolic and ρ_{crit} reflects the radial extension of the ELMs depletion on the profiles, while $\tau_{ped} = 1/f_{ELM}$ was assumed. It should be pointed out that this later assumption takes into account not only the residence time of the impurities but also the recovery of the pedestal profiles after the crash, as well as the possible impurity influx during this phase. The different contributions are currently under investigation.

Once τ is defined, the $n_e \cdot \tau$ grid is built and the non-coronal P_{rad} is calculated as $P_{rad} = L_z\,(T_e, n \cdot \tau) \cdot n_e^2 \cdot c_z$. In the calculations n_e is taken from experimental profiles and c_z is given by the measured impurity concentration profile from the CXRS diagnostic [15]. Figure 3 shows the comparison of the P_{rad} calculations assuming coronal equilibrium over the whole radius in panel (a) and non-coronal condition describe by the model in panel (b). The core radiation is dominated by tungsten while the

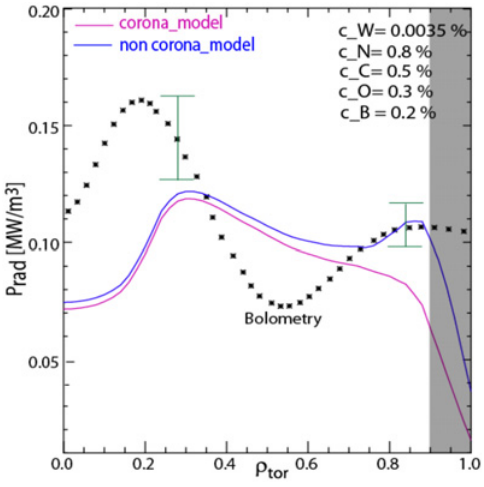

Figure 4. The black dots represent the radiation profile from bolometric measurements. In magenta the calculated P_{rad} using coronal approximation, in blue the calculated P_{rad} using the non coronal model are shown.

edge is dominated by the low-Z impurities (C, O, N). The non-coronal effects affect mainly the low-Z impurities at the edge where the radiation is strongly enhanced. Clearly, under the coronal assumption the radiation power is significantly underestimated. For a correct calculation of the radiated power it is crucial to take into account also the non-coronal effects.

The model is assessed by a comparison with the bolometric measurements as shown in Fig. 4. The mismatch between the calculated and the measured radiation in the core ($\rho_{\mathrm{tor}} < 2$) is attributed to the limited spatial resolution of the bolometry. Only a few lines of sight contribute to the determination of the core radiation profile. Moreover, some of them are also looking at the divertor region where high radiation with steep gradients exist. Hence, the core contribution is affected by large uncertainties. In the outer part of the plasma ($\rho_{\mathrm{tor}} > 0.6$) the experimental reconstruction of the radiation profile is well determined and in good agreement with the calculated radiated power using the non-coronal model. However, in the edge region ($\rho_{\mathrm{tor}} > 0.9$) the results are not reliable due to the experimental uncertainties in the discharges presented here. The radiated power obtained with the non-coronal model is then used in the transport calculations presented in the next section.

3. Transport analysis of radiative cooling experiments

A well established technique to reduce heat loads on divertor target plates is to insert low and medium Z impurities in the plasma to convert the heat flux into radiation and reduced the heat load to the divertor [14]. Nitrogen is a low Z impurity with the properties discussed in the Sect. 2 and it turned out to be indeed a very good candidate for edge and divertor radiation in AUG. An example of radiative cooling experiment by nitrogen radiation in an H-mode with about 14 MW of heating power is shown in Fig. 5.

Figure 5 shows that nitrogen is injected at 2.5 s while the heating power is kept constant since 2.1 s. As expected, the radiative power increases with nitrogen, but surprisingly the plasma stored energy also, by about 15%. This effect is reproducible and attributed to an increase of the pedestal pressure in the presence of nitrogen [5, 6]. The aim of this work is to gain a better understanding of the heat transport under such conditions. For this purpose transport analyses taking into account the spatial distribution of the radiated power have been performed with the TRANSP code [16]. The inputs are the

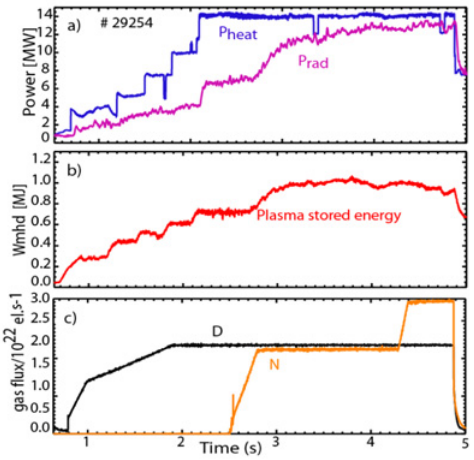

Figure 5. Time traces of key parameters of a typical discharge with nitrogen seeding. a) heating powers in blue, radiated power in magenta. b) Plasma stored energy. c) Gas puff. At 2.5 s nitrogen is introduced.

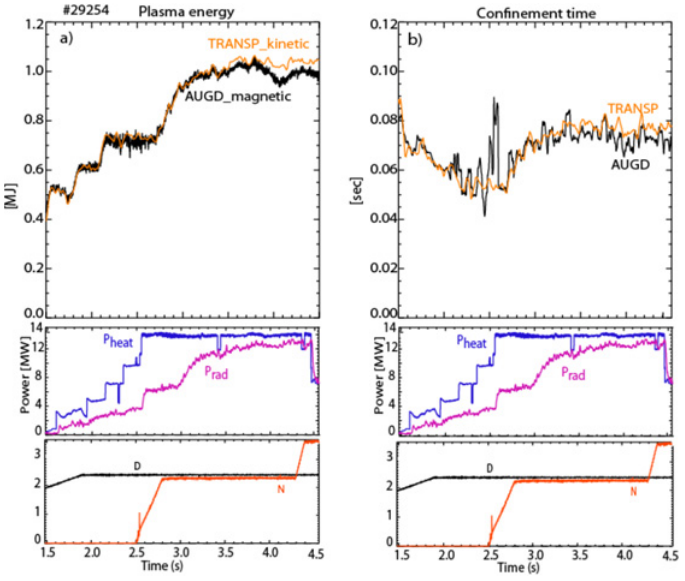

Figure 6. a) Very good agreement of the plasma stored energy between TRANSP calculation (orange) based on kinetic data and AUG estimation based on magnetic data (black). b) Very good agreement between TRANSP calculation (orange) and AUGD (black) also for the energy confinement time. In the plots below heating power and fuelling as shown in Fig. 3.

experimental kinetic profiles and the modelled radiation distribution described in the previous section using the measured impurity concentrations. As shown in Fig. 6a, an excellent agreement for the stored energy is found between the TRANSP determination based on kinetic profiles and the reconstruction based on magnetic data. The energy confinement time also increases with nitrogen as illustrated in Fig. 6b. Also here the TRANSP and experimental results agree very well. The temperature profiles reveal that higher temperatures at the pedestal top are reached during the nitrogen seeded phase as shown in

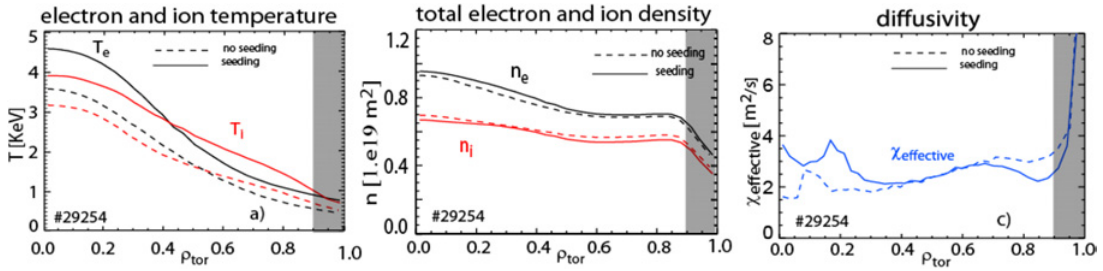

Figure 7. a) Temperature profile, b) density profile. Black for electrons, red for ions. In dashed before the seeding phase, in solid during the seeding phase. Note the higher pedestal temperatures reached during the seeding. c) Effective χ in dashed before the seeding and in solid after the seeding.

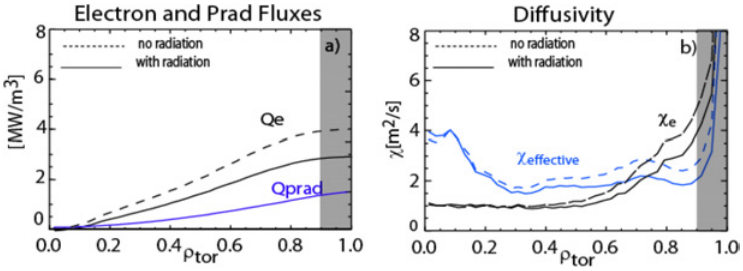

Figure 8. a) In black the electron flux without radiation (dashed) and with radiation in solid. In blue the radiation flux. b) $\chi_{electron}$ (blue) and $\chi_{effective}$ (black) in dashed without radiation, in solid including the radiation.

Fig. 7a. The dashed lines represent the temperature before the seeding, the solid lines during the seeding, in red for the ion, in black for the electron temperature. Note that the pedestal itself is not analysed here, as indicated by the grey area in the plots. Figure 7b shows that the density profiles are weakly affected by the injection of nitrogen. The dilution is rather small because the nitrogen concentration is only 0.8%. The effective heat diffusion coefficient χ_{eff} exhibits similar values before and during the seeded phase, a sign that indeed the seeding is not changing the core transport properties (Fig. 7c).

A sensitivity study of the radiation impact on the transport analysis is illustrated in Fig. 8a. Here the integrated radiative power density Q_{prad} is compared to the electron heat flux Q_e. Q_{prad} is much smaller than Q_e in the central plasma, while it reaches about 30% of Q_e towards the edge. In other words, the radiation is located in the outer part of the plasma, which explains why it has almost no impact of the confinement time. The transport analysis confirms that χ_{eff} varies little in the core when the radiation losses are taken into account or not, Fig. 8b. It should be underlined that high radiation losses in the central plasma would reduce τ_E.

4. High density plasmas with pellets

The repetitive injection of frozen deuterium pellets is a powerful tool for high density operation. The pellet system at AUG was recently upgraded and is now capable of delivering pellets with different sizes, speeds and repetitions rates up to 70 Hz. More details can be found in [16]. An example where the full fuelling capability of the new system has been exploited is shown in Fig. 9. At constant heating power a total number of 70 pellets of the largest available size were injected into the plasma at the maximum rate of 70 Hz with a speed of 572 m/s. The entire ice reservoir was consumed in one go enabling a pellet train of about 1.3 sec. During the pellet phase a high core density is reached and kept until the very last

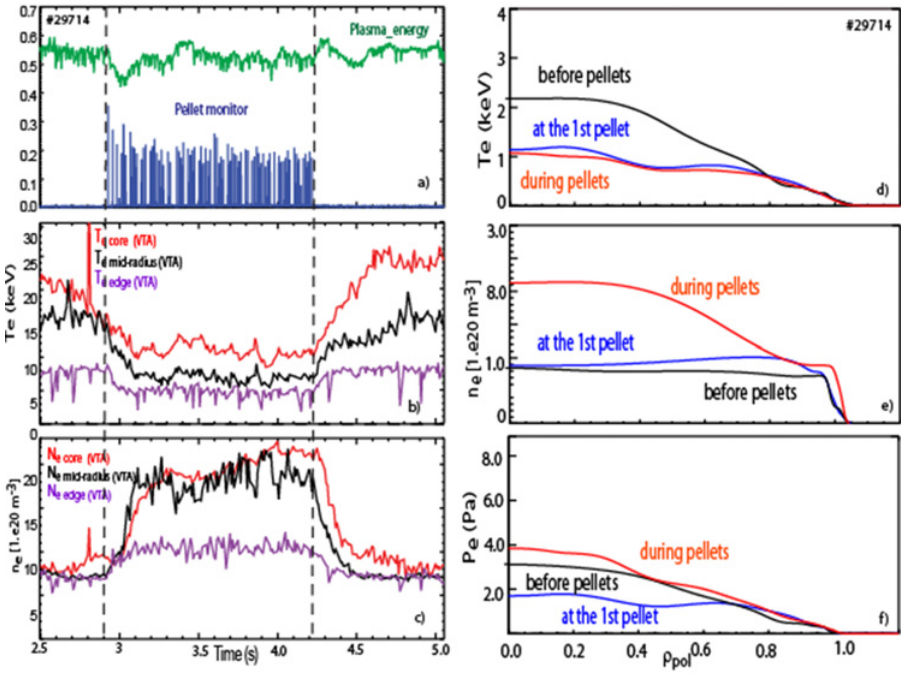

Figure 9. a) Pellet train in blue and stored energy in green. Note the drop in stored energy at the very first pellet. b) Time evolution of temperature, in red the in the plasma core, in black at mid radius, in violet at the edge. c) Time evolution of density, in red in the plasma, in black at mid radius, in violet at the edge. Right column: d) T_e profile, e) n_e profile, f) pressure profiles. For all three plots, black before the pellet injection, blue at the first pellet, red after pellets.

pellet. When the last pellet is consumed all the plasma parameters returned to the initial conditions and the discharge was safely ramped down. Here also, the transport analysis yields a very good agreement between experimental values and TRANSP calculation for the plasma stored energy and the energy confinement time. Both reveal that the stored energy and the confinement time remains constant despite the density increase meaning that τ_E does not depend on the density. This is in contrast to the ITER98 scaling which predicts $\tau_E \approx n_e^{0.41}$ [17].

The attention should be drawn to the transient decrease of the stored energy at the start of the pellet train (Fig. 9a). The drop is caused by the fact that the temperature response is faster than the density response, as indicated by the plots 9b and 9c. The very first pellets induce a drop of the pedestal temperature which propagates quickly toward the centre through the so-called profile stiffness [18]. The density increase starts at the edge with the first pellet but the increase in the core is slow. This is due to the low particle diffusion and to the fact that an increase in density requires a given quantity of particles which can only be delivered by the pellets on a given time scale. The recovery of the stored energy follows the density build up.

This behaviour is illustrated by the profiles of the temperature, density and pressure in Figs. 9d, e and f. The pressure is the same before the pellets and after the transient phase when the density has reached its steady-state value. This is consistent with the constant plasma energy. It should be underlined that due to the drop of T_e caused by the first pellets, the penetration into the plasma of the following pellets is increased which favours the particle fuelling.

5. Conclusion

This paper presents the transport analysis of two key scenarios for the realization of fusion reactors: operation at high radiation and operation at high density. The high radiation scenario is established by impurity seeding. In particular, edge radiation by nitrogen seeding allow to achieve high performance with a cold divertor. Despite the high radiated power, the confinement does not degrade which is attributed to the fact that the main part of the radiation losses occurs in the outer region of the plasma, confirming the prediction for nitrogen. The heat transport in the plasma core does not vary. Furthermore, an enhancement of the confinement time induced by a higher pedestal pressure in the presence of nitrogen is observed. The physics reason is still under investigation. Further core transport studies should also be performed to assess the role of main chamber radiators such as Kr on confinement and assess the limits of such radiative scenarios.

For the high density scenario, pellet fuelling turns out to be a powerful tool and densities up to values required for DEMO have been reached without confinement degradation: under such conditions the confinement time is independent of the density. The validity of this result will be assessed on a wider range of experimental conditions. These results can contribute to an improvement of the scaling law for the energy confinement time.

References

[1] F. Wagner, Plasma Phys. Control. Fusion, **49**, B1–B33 (2007)
[2] H. Zohm, Plasma Phys. Control. Fusion, **38**(2):105 (1996)
[3] R. Neu et al., J. Nucl. Mater., **367–370**, 1497–1502 (2007)
[4] A. Kallenbach et al., Nucl. Fus., **52**, 12, 122003 (2012)
[5] G. Tardini et al., Plasma Phys. and Control. Fusion, **55**, 015010 (2012)
[6] J. Schweinzer et al., Nucl. Fus., **51,** 113003 (7pp) (2011)
[7] P. T. Lang et al., Nucl. Fus., (2013) (submitted)
[8] J. Wesson, *Tokamaks*, Oxford Science Publications, Oxford (1997)
[9] J. C. Fuchs et al., 21st EPS Conference on Controlled Fusion and Plasma Physics (1994)
[10] U. Samm et al., J. Nucl. Mater., **176–177**, 273 (1990)
[11] D. Post, Phys. Plasmas, **2**, 2328 (1995)
[12] H.P. Summers, *Atomic data and analysis structure user manual* (1994) `http://open.adas.ac.uk/`
[13] T. Puetterich et al., Nucl. Fus., **50**, 025012 (2010)
[14] A. Kallenbach et al., Plasma Phys. and Control. Fusion, **55**, 124041 (2013)
[15] E. Viezzer et al., Review of scientific Instruments, **83**, 103501 (2012)
[16] A. Pankin et al., Computer Phys. Communications, **159**, 157–184 (2004)
[17] ITER Physics Basis, Nucl. Fus., **39**, Chap. II, 2208, Table 5 (1999)
[18] F. Ryter et al., Plasma Phys. Control. Fusion, **48** (2006) B453–B463